A snapshot of the vast array of diamagnetic CEST MRI contrast agents

NMR BIOMED Special Issue CEST – Diamagnetic CEST agents

Dario Livio Longo[1], Antonella Carella[1], Alessia Corrado[1], Elisa Pirotta[1], Zinia Mohanta[2,3], Aruna Singh[2,3], Julia Stabinska[2,3], Guanshu Liu[2,3], Michael T. McMahon[2,3]

[1]Institute of Biostructures and Bioimaging (IBB), National Research Council of Italy (CNR)
Via Nizza, 52, 10126 - Torino – Italy
[2]F.M. Kirby Center for Functional Brain Imaging, Kennedy Krieger Institute, Baltimore, Maryland, USA.
[3]Department of Radiology, Johns Hopkins University School of Medicine, Baltimore, Maryland, USA.

Main

Introduction

A core feature of CEST imaging is the capability of amplifying the signal from low-concentration diamagnetic compounds through their interactions with water, thus enabling their detection at higher spatial resolution than conventional spectroscopic methods. Additionally, this signal amplification is based on continuous transfer of saturation between protons in specific molecules and water protons, achieved by simply adding a frequency-selective presaturation pulse to an imaging sequence. This allows CEST imaging to be performed on standard clinical MRI scanners without hardware modifications. For CEST MRI to become a widely used technology within radiology departments, a major need is to identify which compounds can be detected in the tissues of interest. Most CEST applications focus on endogenous molecules that can be found in the human body or chemical substances that can be administrated externally to generate exogenous CEST contrast. In general, CEST agents can be divided into two groups based on their chemical shift: paramagnetic CEST agents (paraCEST), which contain metallic ions that induce large chemical shifts, and diamagnetic chemical CEST agents (diaCEST) with exchangeable protons, i.e. -OH, $-NH_2$, -NH, which are either naturally occurring compounds or synthetic contrast agents with chemical shifts within 12 ppm from water resonance. Because of their excellent biocompatibility and biodegradability, a number of diaCEST agents and their potential applications have been widely investigated and reported in multiple preclinical and clinical studies. As a result, the list of

diaCEST probes that could potentially be used in clinical settings has grown tremendously since the seminal works of Balaban, van Zijl and colleagues [1-6], and our previous diaCEST agent review [7]. The purpose of this review is to provide an updated overview of the various types of diamagnetic compounds suitable for molecular imaging in the context of their suitability for clinical CEST MRI applications. We do not extensively discuss endogenous CEST agents, which have been summarized as key ones will be described by others in this NMR in Biomedicine issue, instead we focus on exogenous diaCEST probes, which are particularly promising candidates for clinical translation because of their safety profiles and potential to highlight a wide range of pathologies.

1. Small molecules

1.1 Sugars

Glucose is a key marker of the dysregulated metabolism in solid tumors. Consequently, imaging-based approaches that allow to detect the increased glucose uptake in cancer cells are needed for improving cancer diagnosis. The FDG-PET technique relies on the use of radiolabeled glucose and nowadays is considered the gold standard for assessing the upregulated glucose metabolism in tumors. However, ionizing radiations and limited availability of PET scanners have prompted the quest for alternatives to the radiolabeled glucose. Recently, the CEST technique has been proposed for detecting a variety of exogenously administered, unlabeled glucose and glucose analogues (glucoCEST) [8-10].

D-glucose was firstly investigated as potential alternative to FDG owing to its molecular structure possessing a large number of hydroxylic mobile protons and a high safety profile (**Fig. 1a**). In vivo studies on two human breast cancer murine models (MDA-MB-231 and MCF-7) demonstrated the detectability of this molecule within the MRI-CEST technique and showed the capability to discriminate between different tumor phenotypes based on the differences of the measured glucoCEST contrast [10]. Similar results were observed by Walker-Samuel and coworkers, on two subcutaneous human colorectal tumour mouse models (LS174T and SW1222 cancer cells) with the glucoCEST contrast that correlated well with the FDG-PET findings. In addition, this study highlighted that the measured glucoCEST contrast might not only report on cellular uptake and metabolic activity but also on the vascular delivery of glucose, thus increasing the complexity of the origin of the observed contrast [9]. Studies are ongoing to shed light on the source of the observed glucoCEST contrast (**Fig. 1b**). To date, only one study by Capozza and coworkers compared the glucoCEST contrast to the FDG-PET technique to monitor response to therapy, in this study, they monitored changes in metabolism in a breast cancer murine model treated with two different therapies. The findings demonstrated that the glucoCEST technique is more sensitive to monitor the therapeutic

effect following Doxorubicin administration, with a marked decrease of the glucoCEST contrast that was associated to a reduction of the tumor growth, whereas the FDG-PET is not able to report on any difference (**Fig. 1c**). [11].

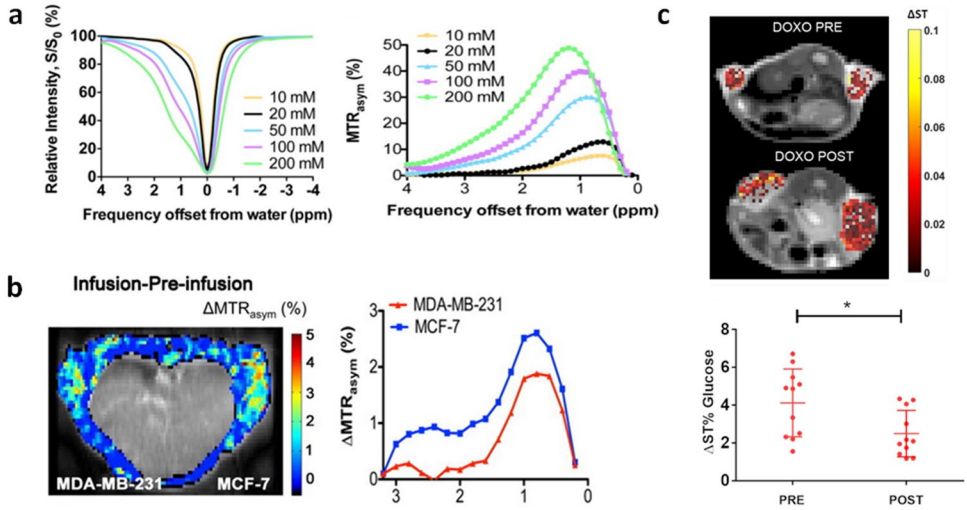

Figure 1. a) Z-spectra (left) and MTR_{asym} (right) as a function of concentration at pH 7.3 for B_1=1.6 µT. b) Left: GlucoCEST difference map: ΔMTR_{asym} = MTR_{asym}(Infusion)–MTR_{asym}(Pre-infusion). The intensity of the internal body was thresholded out because it contains moving areas (lungs and heart) that have large magnetic susceptibility differences with surrounding tissues, which complicates difference imaging. Tright: the ΔMTR_{asym} profiles of MDA-MB-231 and MCF-7. [Reprinted from 23074027] c) Top: representative glucoCEST ΔST% maps of 4T1 tumor–bearing mice, before and after treatment. Data are reported as the difference (ΔST%) between the ST effect before and after the intravenous glucose injection. Parametric maps are overimposed to T_{2w} anatomical images and glucoCEST contrast is shown only in the tumor region. Bottom: graph showing individual GlucoCEST contrast (and mean ± SD) obtained injecting glucose at 3 g/kg dose via intravenous bolus (n = 6 mice). Data are reported as the variation (ΔST%) between the ST effect post-injection minus the ST effect pre-injection. Paired t-test *p = 0.0216. [Reprinted from[11]]

In contrast to the radiolabeled FDG molecule, D-glucose can be metabolized, therefore analogues of this molecule have been investigated as non-metabolizable alternatives. Rivlin et al. considered the 3-O-Methyl-D-glucose (3OMG), a synthetic nontoxic and nonmetabolizable derivative of glucose. Since the 3OMG uptake and entrapment inside the cancer cells is comparable to that of the FDG molecule, they observed a marked and prolonged glucoCEST contrast in several murine tumor models [12]. However, when native D-glucose and 3OMG were compared side by side under the same experimental conditions, administered doses and on the same tumor model, they provided similar

glucoCEST contrast, even with their different metabolic fates [13]. Another sugar, xylose, can maintain high concentration in tissues because of its slow metabolism. Furthermore it is able to pass through the BBB (blood-brain barrier). Wang and coworkers demonstrated in vivo the glucoCEST contrast efficiency of xylose upon bolus injection in rat brain [14]. Another non-metabolizable glucose derivative. 2-DG, was detected in the brain of healthy rats, although the lower safety profile of this molecule poses some challenges for the high doses requested by the CEST technique [15]. Maltitol, a non-metabolizable sugar was investigated in vivo demonstrating a moderate accumulation and glucoCEST contrast in the extracellular space of rat gliomas [16]. Myo-inositol is another sugar which has displayed promise as well [17].

1.2 Amino acids and creatine

Amino acids are key building blocks for proteins and are actors in various processes including skeletal muscle function, atrophy and tumor growth. Amino acids also play key roles in cell signaling, cell homeostasis, gene expression and a number of important pathways. So amino acid detection could reveal quite a bit about pathology. There are a number of labile protons on the 20 natural amino acids which might be exploitable for CEST studies. Their detection was envisioned in the earlier works of Balaban and colleagues [4], however more recently investigators have focused on glutamate, arginine, and alanine which are well detected and can be also present at mM concentrations in tissue[18-21]. For example, it was discovered that glutamate possessed amine protons which are relatively slow compared to other amino acids enabling Glutamate CEST (GluCEST) detection after infusion [20]. This probe is present at mM concentrations in the brain, allowing the use of GluCEST for detecting elevated concentrations in the striatum and motor cortex in a mouse model of parkinson's disease [22]. This probe may also hold promise for epilepsy and other pathologies[23, 24], and is the subject of a review later in this issue. Alanine is also present at mM concentrations in tissue and has suitable exchange rates for detection as well [18, 25]. Arginine possesses guanidyl amine protons which are well suited for detection, and this agent has been used for a few different types of contrast applications. For example, pH sensors were built around arginine into hydrogels suitable for transplantation of cells to monitor their location and their survival [26]. Creatine is synthesized from the amino acids glycine and arginine and also possesses guanidyl protons well suited for detection and present at high concentrations in skeletal muscle along with its phosphorylated derivative phosphocreatine [27-31]. It is also a common nutritional supplement that can be detected after administration [32]. Further discussion of this agent can be found in a later review in this issue as well.

1.3 Porphyrin metabolites

Porphyrin biosynthesis is an important pathway that is involved in a number of biological processes including angiogenesis. As the porphyrins are also one of the most aromatic compounds produced by the body with large ring currents, it was expected that these could also possess excellent CEST properties as well. The inner ring NH protons are labile and can be tuned to maximize CEST contrast depending on the substitution of the porphyrin ring as we have shown recently [33]. These are highly upfield shifted, resonating at ~16 ppm higher field than NH resonances on lysine rich peptides with these unusual shifts due to the effect of "ring currents" formed by the precession of 18 π-electrons in the porphyrin ring. A series of natural porphyrins and a few artificial porphyrins were tested with the substitution of the porphyrin ring impacting the exchange properties quite substantially. Other artificial porphyrins appear promising as well [34]. Porphyrins might present unique challenges for in vivo imaging studies as they tend to ligate metals at their axial site and self-aggregate. However, they might also present unique opportunities for medical applications such as combining MRI with optical image-guidance of surgeries [35] and photodynamic therapies [36] which employ similar compounds.

1.4 Pharmaceutical excipients

Pharmaceutical excipients should be molecules endowed with high or very high safety profiles, making these interesting prospects based on the high concentrations often needed by CEST agents for in vivo detection. Longo and coworkers performed i*n vivo* experiments on murine breast (TS/A) and melanoma (B16) tumor models on a wide range of excipients, with meglumine, N-acetyl glucosamine and ascorbic acid yielding the highest CEST contrast enhancement [37].

2. Macromolecules and superstructures

2.1 Dextran and Glycogen

Small molecules possess few mobile protons in exchange with water, therefore, their efficiency in generating a CEST contrast is a limiting factor. To overcome this limitation, several strategies have been pursued by exploiting or macromolecular agents possessing a larger number of mobile protons or nanosized systems endowed with water molecules entrapped inside the liposomes' cavity. Several polysaccharides have been exploited as diaCEST agents, including dextran[38, 39], glycogen[40, 41], starch[42], and other sugar-based polymers[43]. Like monosaccharides such as glucose, polysaccharides also have a strong CEST signal at around 1 ppm, attributed to hydroxyl protons. The advantage of polymeric CEST agents is their much-enhanced sensitivity compared to small molecular agents. Our group has extensively developed dextran as CEST agents. Dextran is considered as an ideal polymeric CEST agent because dextrans are biologically inert and have been used in the clinic for many decades.

Dextrans are also available at different sizes, permitting them to be used in different biomedical applications. For example, intravenously administrated large dextrans (e.g., 150 kDa) are restricted in the blood circulation and can be exploited as intravascular agents [44]. In contrast, dextrans of smaller size are more suitable as an imaging moiety to construct targeted CEST MRI agents because they are easier to permeate to the tumor parenchyma [39, 45]. Another good example is the dextran-based PSMA receptor imaging that we have developed and demonstrated in experimental prostate tumors (**Fig. 2**)[39]. A μM detectability was accomplished for detecting *c.a.* $5x10^6$ PSMA receptors per tumor cell, which is almost impossible for small molecular MRI agents.

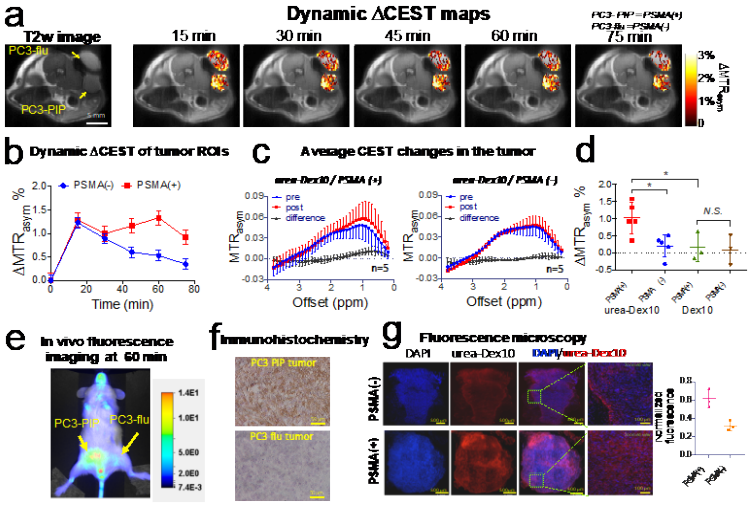

Figure 2. Changes in the dynamic CEST signal in PSMA(+) and PSMA(–) tumors. **a**) T2-weighted image and dynamic CEST maps at 1 ppm after the injection of 375 mg/kg urea-10KD-dextran (injection volume =100 μL). **b**) Mean changes in the CEST signal in PSMA(+) and PSMA(–) tumors in one of the mice for which time dependence was measured. CEST signal enhancement was quantified by $\Delta MTR_{asym} = MTR_{asym}(t) - MTR_{asym}(t=0)$, where the error bars are the standard errors of the CEST signal of all the pixels in each tumor. All CEST images were acquired using a 1.8 μT and 3-second-long CW pulse. **c**) Average CEST signal in the tumor for five mice before (blue) and one hour after (red) the injection of urea-Dex10. The signal difference is shown in black. Error bars are standard deviations of the CEST signal of all five tumors. **d**) Bar plots showing the mean changes in CEST signal as quantified by ΔMTR_{asym} (1 h) in each type of tumor (n = 5 and 3 for urea-Dex10 and non-targeted Dex10, respectively). * : $P<0.05$ (Student's t-test, two-tailed and unpaired). **e**) In vivo fluorescence image of a representative mouse showing a distinctive tumor uptake of urea-Dex10 at 60 minutes after injection. **f**) Sections of PSMA(+) PC3-PIP (top) and PSMA(–) PC3-flu (bottom) ttumorsstained with anti-PSMA. Images were acquired at 40× magnification. **g**) Fluorescence microscopy of nuclei (blue, stained with DAPI) dextran (red, NIR-600-labeled). Scale bar= 500 μm for the left three panels and 100 μm for the most right panels, which are the zoomed view of the area enclosed in the dashed green box in the image on the left. On the right, a scatter plot shows the comparison of the normalized mean fluorescence intensity of three different fields of view in the tumors. Reproduced from [39].

Of note, recent studies have shown that the relayed Overhauser effect (rNOE) effect may also be utilized to detect polysaccharides such as glycogen by their macromolecule nature in addition to the CEST signal at 1 ppm (OH protons). In particular, the saturation on glycogen aliphatic protons is

transferred to a neighboring hydroxyl proton and subsequently to water via proton chemical exchange between glycogen hydroxyl protons and water.[41, 46] Such an approach enables noninvasive mapping of glycogen using a more distinguishable, pH-insensitive CEST MRI signal.

To accelerate towards potential clinical translation, Consolino and collaborators have focused on the FDA-approved plasma volume expanders as macromolecular CEST agents. Both dextran70 and voluven showed in vivo a marked CEST contrast in a breast tumor murine model, with comparable contrast enhancement properties to that observed with a blood-pool gadolinium-based contrast agent [42].

2.2 Liposomes, Hydrogels

Another strategy is based on the encapsulation of high payloads of diaCEST agents into liposomes. Our first attempt included encapsulating Poly-L-Lysine, L-arginine and glycogenand injecting these into the footpad to watch lymphatic delivery of these into the popliteal lymph nodes of mice [19]. We have also developed a barbituric acid (BA) liposome (BAL) with CEST contrast at 5.0 ppm and have tested this both for monitoring intravenous delivery to colon tumors [47] and vaginal distribution and retention [48]. BA has also been dispersed in hydrogels with contrast at 5.0 ppm and -3.4 ppm which are related to the amount of liposomal drug (BA) and to the amount of hydrogel following hydrogel transplantation into the tumor area [49]. To overcome the sensitivity limitations of the glucoCEST approach, liposomes entrapped with glucose or 2DG have been investigated, too. The observed results demonstrated that the encapsulation into the liposomes can lower the fast chemical exchange rate of the hydroxylic protons and thus provide high glucoCEST contrast [50].

Supramolecular agents such as hydrogels, have been considered, too, thanks to the large number of exchanging protons. Such macromolecular systems can be exploited to deliver anticancer drugs such as Pemetrexed and to monitor their accumulation within the tumor, acting as a theranostic agent [51]. Hydrogels are also widely used as biological scaffolds to repair soft tissues after injuries, so the hydrogels in vivo distribution, biodegradation and cell survival can be monitored over time by looking to the CEST contrast, as demonstrated after implantation of hepatocytes into mice and comparing with bioluminescence reporter gene expression [52] and also implanting these into the stroke cavity in a rat model [53].

2.3 Polynucleotides, Poly Amino acids and Peptides

Some of the earliest work on CEST agents involved the identification of macromolecules which are work well as CEST agents including the seminal work by van Zijl and colleagues [3]. The first of these identified included the Poly amidoamine dendrimer and Poly-L-Lysine which possess amine and amide protons well-tuned for detection between 3 to 3.5 ppm from water. More recently salicylate based dendrimers have been prepared with superior chemical exchange properties [54]. Poly nucleotides can also possess excellent properties for detection, depending on their nucleotide sequence [5]. Furthermore, a wide range of peptide CEST agents have been designed at this point including the Lysine Rich Protein [55] and arginine rich and threonine rich peptides [56]. Due to the outstanding promise displayed by these agents, the many variations will be covered extensively by Gilad and others in another review in this issue.

3. pH imaging agents

MRI is one of the primary means to measure tissue pH, and can be used to asses the intra- and/or extracellular tissue pH [57]. Proton exchange is particularly sensitive to the acid-base equilibrium, in fact Balaban and co-workers reported CEST agents (shortly after his initial discovery) as pH sensors. Both paramagnetic CEST (paraCEST) agents [58-64] and diamagnetic CEST (diaCEST) [65-72] agents have been reported as pH sensors. Multi-color detection is an important advantage of CEST agents for pH imaging, as this allows use of ratiometric imaging to compensate for changes in agent concentration [65]. In this section, we will go over two classes of diaCEST agent that have shown promise for ratiometric pH mapping: the triiodobenzenes and the imidazoles.

3.1 Iodinated contrast media

Iodinated X-ray/CT contrast agents have been thoroughly investigated for CEST MRI due to their larger shifted amide protons and to their very high safety profiles, even at high doses [73]. In recent years, several iodinated molecules, including iopamidol, iobitridol, iodixanol, iopromide and iohexol have demonstrated excellent results in terms of MRI-CEST contrast efficiency and as pH responsive contrast agents. In particular, the development of contrast agents able to report on tissue pH is of clinical relevance, since several pathologies are associated with an altered acid-base balance, including, ischemia, renal failure and cancer [74-77]. The exploitation of iodinated contrast agents as MRI-based contrast agents was firstly proposed by Aime and coworker as T2 exchange agents [78] and then demonstrating interesting MRI-CEST properties in vitro with the use of iopamidol [79]. A further step was provided by Longo and coworkers by exploiting the two not-chemical equivalent amide groups of Iopamidol for a concentration-independent ratiometric approach to provide pH responsiveness in the physiological pH range and demonstrating in vivo the capability to obtain

highly spatially resolved pH maps in the murine kidneys at high magnetic field strengths (7T) [80]. A throughout characterization of the pH responsive properties of Iopamidol was performed by Sun et al. showing high accuracy in the pH range between 6.0 and 7.5 even at moderate high fields (4.7 T, **Fig. 3a**) [81]. Later on, Longo et al. demonstrated tumor extracellular pH mapping with the use of Iopamidol [82]. In addition, they proposed a novel approach for pH mapping even for molecules endowed with only one exchanging proton, such as Iobitridol (a non-ionic, monomeric, low-osmolar iodinated contrast medium), by exploiting the ratio of two different radiofrequency irradiation power levels (**Fig. 3b**). This novel approach provided comparable pH values to those provided by iopamidol in both tumor and renal pH images. In the same years, Pagel et al. showed that Iopromide, a low osmolar, non-ionic iodinated contrast medium with a similar chemical structure to Iopamidol, can be exploited as a pH responsive contrast agent for mapping tissue pH, dubbing the approach acidoCEST (**Fig. 3c**) [83]. The comparison of Iopromide and Iopamidol as pH responsive agents showed that Iopromide can produce a pH measurement with a higher dynamic range, whereas iopamidol can produce a more precise pH measurement, although the calculated pH values were not significantly different [84].

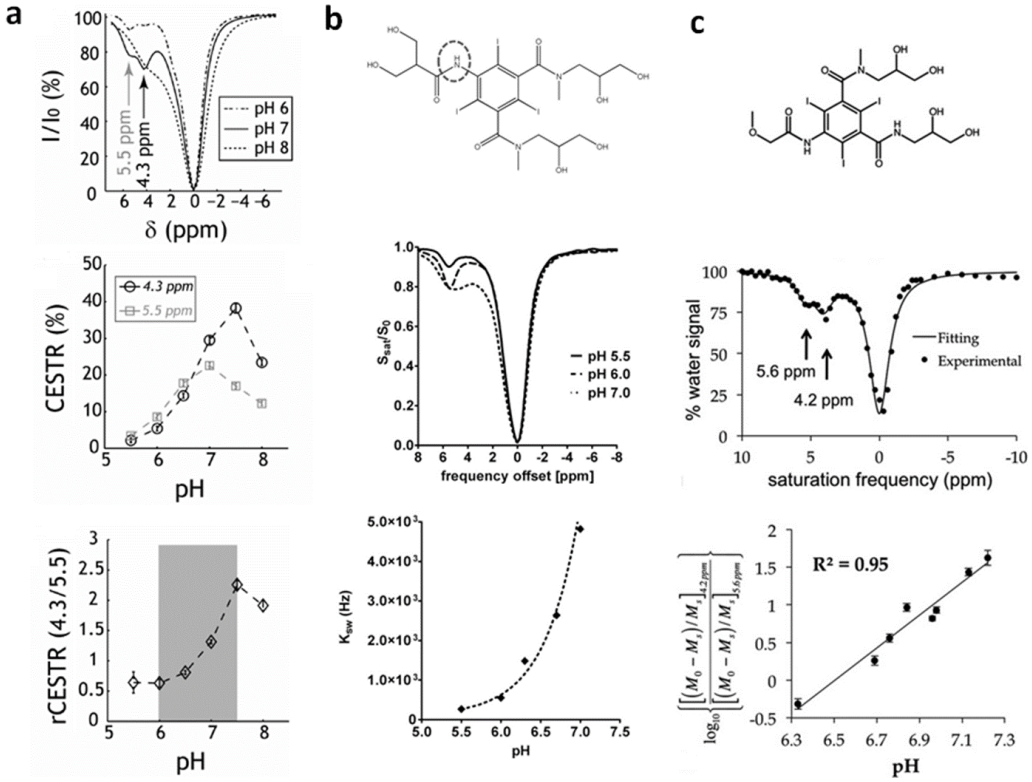

Figure 3. **Comparison between Iopamidol, Iobitrol and Iopromide ratiometric pH MRI**. a) Top: Iopamidol chemical structure. Middle: Z-spectra for representative pH of 6, 7 and 8 (B_1 = 2.5 μT, TS = 5 s) at room temperature. Bottom: Ratiometric CEST analysis is sensitive to pH ranging from 6 to 7.5. [Adapted from [81]]. b) Top: Iobitridol chemical structure with a single amide proton group. Middle: CEST spectra of 30 mM iobitridol solution at pH of 5.5 (solid line), 6.0 (dashed line), and 7.0 (dotted line). The reduction in MRI signal from bulk water signal upon selective irradiation at 5.6 ppm is pH sensitive (RF saturation power = 3 μT × 5 s, T = 310 K,

B_o = 7 T). Bottom: numerically solved pH-dependent chemical exchange rate for labile protons at 5.6 ppm. [Reprinted from [82]] c) Top: the chemical structure of iopromide. Middle: a CEST spectrum of 200 mM iopromide at pH 6.69 and 37.0°C with saturation applied at 2 μT for 5 s. Bottom: a $\log_{10}$ ratio of the two CEST effects is linearly correlated with pH from pH 6.3 to pH 7.2. [Reprinted from [83]]

Iodixanol, a dimeric iso-osmolar, non-ionic, iodinated radiocontrast agent was exploited by Arena and collaborators showing another ratiometric approach for pH imaging without the need of two different resonant frequencies or of a continuous-wave irradiation when using a double angle pulsed saturation scheme [85]. Recently, also Iohexol, another iodinated, non-ionic, low osmolar contrast agent was investigated within the Spin-Lock approach as a competitive method for generating contrast in comparison to the CEST one [86]. Most of these contrast media have been compared in vivo upon extravasation and accumulation in the extracellular space in tumors for their efficiency to generate MRI-CEST contrast in respect to the CT attenuation properties. Overall, a comparable CEST contrast was observed among all the investigated molecules with a strong and positive correlation between CT and CEST-MRI derived contrast enhancement [87].

Over the years, gadolinium has always been considered the gold standard in the MRI contrast enhanced approach, although serious clinical issues have been identified including contraindicating Gd-enhanced MRI for patients with poor kidney function due to risk of developing nephrogenic systemic fibrosis [88, 89] and Gd-contrast agents accumulate in several organs over many years [90-93]. Iodinated contrast media are an alternative which has been investigated using the MRI-CEST approach. In a recent study, Anemone et al. demonstrated similar pharmacokinetic profiles and contrast enhancement properties between Gd-based and iodinated molecules, with T1-weighted or CEST technique, respectively [94]. Interestingly, after intravenous injection, several iodinated agents showed similar perfusion properties within a breast tumor murine model, with a marked correlation in both contrast and spatial enhancement and spatial showed by iopamidol.

3.2 Imidazole pH agents

Heterocycles such as imidazole and its analogues can have highly shifted labile protons due to the presence of pi electrons and a capacity for intramolecular hydrogen bonding. These chemical features endow these compounds with NMR properties which are pH responsive. For instance, certain N-alkylated imidazoles including 2-imidazole-1-yl-3-ethoxy-carbonyl propionic acid (IEPA) and 2-imidazole-1-yl-succinic acid (ISUCA) have been found to be important MRS pH sensing agents owing to the chemical shift of the C-2 proton [95, 96]. We investigated various imidazole analogues and compared their N-H exchangeable protons for pH sensing by implementing CEST. Free imidazole (**1 in Fig. 4**) does not provide CEST contrast at neutral pH due to its fast exchange rate with water. Based on the knowledge that histidines in the catalytic site of serine proteases

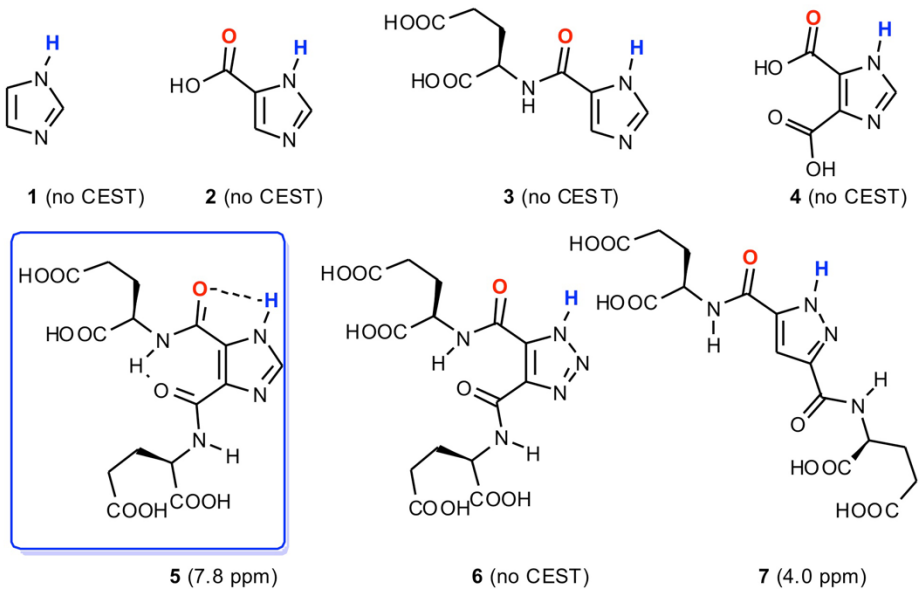

Figure 4. Select azole derivatives analysed for their CEST properties (Reprinted from [97]).

showed a decreased exchange rate of the imidazole N-H groups and chemical shifts as far as 13 ppm downfield from water by virtue of their hydrogen bonding network [98, 99], we decided to try and prepare an imidazole compound with a suitable intramolecular hydrogen bonding as a CEST agent. We have synthesized and tested over 25 variants at this point, and have found 4,5-bis[(Glu)carbonyl]-*1H*-imidazole,(I45DC-Glu_2, **5** in **Fig. 4**) which generates strong CEST contrast at 7.5 ppm at neutral pH [97]. The number of nitrogens in the ring and substituents attached to this were critical for stabilizing the conformation and enabling CEST contrast production [100, 101]. Moreover, the two labile proton types in this molecule, high pH sensitivity and water solubility make it a good candidate for ratiometric pH measurements. The mechanism of contrast enhancement is expected to be similar to the behaviour seen previously and attributed to changes in conformation as the pH drops [100]. We have tested this agent *in vivo* and succesfully mapped the pH of mouse kidneys [97]. The imidazoles are generally considered to be well tolerated enabling their usage in the clinic, with similar compounds such as flumizole, dacarbazine and cimetidine and a number of others having LD50s of 500 - 2,500 mg/kg and used as antiinflammatories, H2 antagonists, anticancer, anticonvulsants, antifungals or to treat hypertension. [102, 103] This combination of factors has inspired us to further test our imidazole agent for pH mapping in certain renal diseases and injuries including due to urinary tract obtruction, methyl malonic acidemia with this work ongoing.

3.3 Applications of pH imaging

One of the main focusses of pH mapping studies is applying these for cancer imaging because of the well known tumor extracellular acidification upon the combined effects of dysregulated metabolism, hypoxia and reduced perfusion [75, 76, 104, 105]. Indeed, a number of early studies were performed to characterize the pH of tumors using CEST MRI [77, 83, 84]. A first in vivo demonstration of the relationship between upregulated glycolysis and tumor acidosis via CEST imaging was provided by Longo and coworkers, reporting a strong correlation between ^{18}F-FDG uptake and tumor extracellular pH (pHe) by combining PET and MRI-CEST pH imaging in a breast tumor murine model [106]. Nowadays, high resolution tumor pH maps are achievable within a reasonable acquisition time that allows to obtain information on spatial tumor pH heterogeneity (**Fig. 5**).Tumor pHe mapping can be exploited for assessing response to anticancer therapies that can alter the homeostasis of tumor acidosis. Drugs targeting the glycolytic metabolism are expected to affect the extracellular tumor

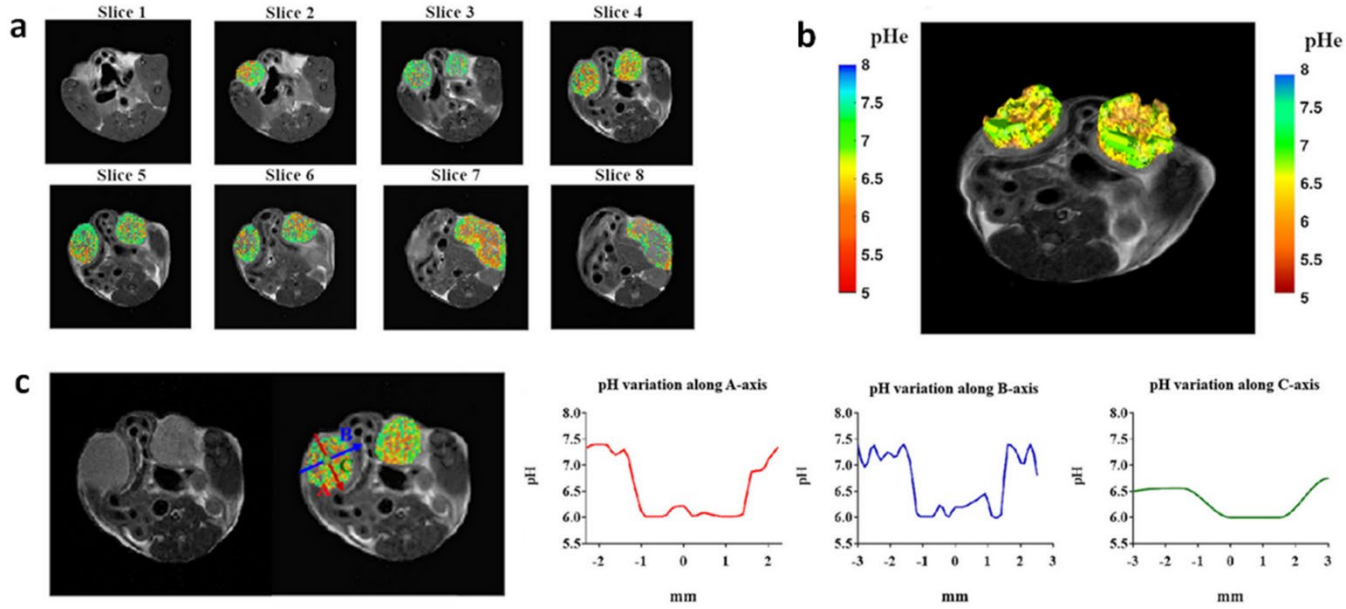

Figure 5. Comparison between Iopamidol, Iobitrol and Iopromide ratiometric pH MRI. a) Top: Iopamidol chemical structure. Middle: Z-spectra for representative pH of 6, 7 and 8 (B_1 = 2.5 μT, TS = 5 s) at room temperature. Bottom: Ratiometric CEST analysis is sensitive to pH ranging from 6 to 7.5. [Adapted from [81]]. b) Top: Iobitridol chemical structure with a single amide proton group. Middle: CEST spectra of 30 mM iobitridol solution at pH of 5.5 (solid line), 6.0 (dashed line), and 7.0 (dotted line). The reduction in MRI signal from bulk water signal upon selective irradiation at 5.6 ppm is pH sensitive (RF saturation power = 3 μT × 5 s, T = 310 K, B_o = 7 T). Bottom: numerically solved pH-dependent chemical exchange rate for labile protons at 5.6 ppm. [Reprinted from 25238643] c) Top: the chemical structure of iopromide. Middle: a CEST spectrum of 200 mM iopromide at pH 6.69 and 37.0°C with saturation applied at 2 μT for 5 s. Bottom: a $\log_{10}$ ratio of the two CEST effects is linearly correlated with pH from pH 6.3 to pH 7.2. [Reprinted from [83]]

acidification [107]. This has been showed in vivo in a breast cancer murine model upon dichloroacetate administration that can revert the dysregulated glycolysis. Interestingly, tumor pH values increase strongly after dichloroacetate treatment and were confirmed by the decrease of the lactate levels, showing the early response to treatment. However, 15 days after the tumor became resistant, lactate levels were similar between untreated and treated groups and tumor pH imaging demonstrated the onset of resistance to the drug [108]. CEST pH imaging was also exploited to evaluate, in combination with FDG-PET studies, the early response to metformin on a preclinical model of pancreatic cancer [109]. However, although CEST-MRI did not report any increase in tumor pHe, likely reflecting the mechanism of action of metformin, the following PET analyses detected a reduction in glucose uptake, by confirming an alteration of the glucose uptake. Since tumor acidosis is nowadays considered as one of the leading causes of cancer aggressiveness and invasiveness, MRI-CEST pH imaging has been investigated as a potential imaging biomarker of the metastatic potential. Anemone and colleagues investigated several breast cancer cell lines with different metastatic potentials, showing that cell lines with higher invasiveness (larger and higher number of lung metastases) reflected an increased tumor acidity and heterogeneity, whereas less aggressive tumors resulted in lower tumor acidosis and smaller and reduced lung metastases (**Fig. 6**) [110]. Iopamidol CEST pH imaging has also been exploited to confirm the presence of acidic niches in lymph nodes, providing precious

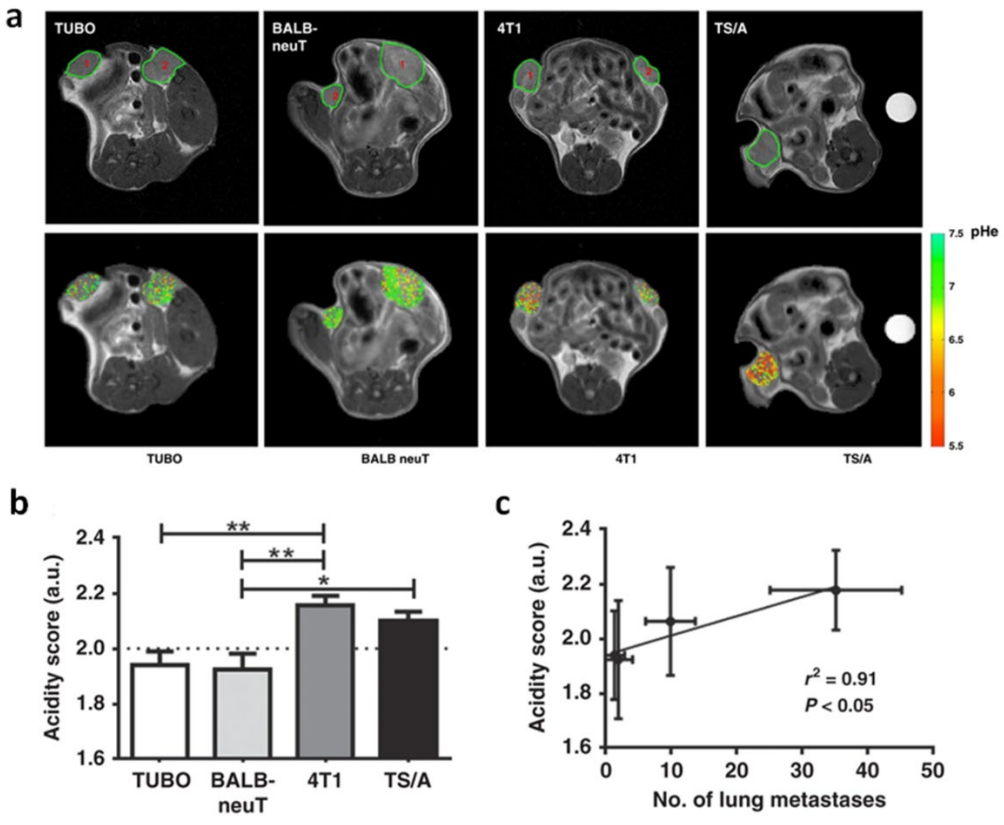

Figure 6. Anatomical images of acidic tumour environment and pHe in vivo correlation with lung metastasis a) Top: anatomical T_{2w} images of TUBO, BALB-neuT, 4T1 and TS/A representative tumours. Bottom: **r**epresentative tumour extracellular pH maps for TUBO, BALB-neuT, 4T1 and TS/A tumours. b) Acidity score calculated for TUBO, BALB-neuT, 4T1 and TS/A tumour. $*P < 0.05$ and $**P < 0.01$. c) Correlation between acidity score and number of lung metastases ($r^2 = 0.91$, $*P < 0.05$). [Reprinted from [110]]

information about the physiological microenvironment and its influence in immune cells activation and glycolytic metabolism maintenance [111]. In addition, Jones and colleagues provided the clinical translation proof of iopamidol-based pHe mapping by measuring pHe values in ovarian and in breast cancer patients with a clinical MRI 3T scanner [112]. Overall, these results highlight that iopamidol-based tumor pH imaging can be considered useful for characterizing tumor aggressiveness and to assess response to anticancer therapies.

The acid-base balance plays a fundamental role in kidneys, consequently, pH imaging of kidneys is expected to provide useful information regarding renal functionality. Some of the first evidence of altered renal pH values in a preclinical severe but transient acute kidney renal injury model were provided by Longo et al. showing marked pH alterations that restored to normal basal pH values after a recovery period [113]. In another study, upon single-kidney ischemia-reperfusion injury, iopamidol-based renal pH imaging was capable to distinguish between the clamped and the contralateral kidneys and to monitor the renal pH evolution in a moderate and in a severe injury model [114]. Additionally, Irrera and coworkers reported a dynamic CEST approach for assessing both renal perfusion and pH homeostasis in an acute ischemia-reperfusion injury murine model. Iopamidol was injected and exploited for providing a dual reading of both perfusion and pH, with a marked reduction of renal filtration and increased pH values for the clamped kidneys in comparison to the contralateral ones [115]. Consequently, the dynamic CEST approach was able to assess and distinguish the renal function between the healthy and the clamped kidneys and these results correlated with the perfusion values obtained with a DCE-MRI approach upon gadolinium-based contrast agent injection in the same mice. Another study tested iopamidol based perfusion and pH maps for differentiating healthy kidneys from mild and severe chronic kidney disease in a transgenic mouse model of methyl malonic acidemia [116]. Three metrics were found to correlate with mouse weight including contrast magnitude, filtration fraction and range in pH values across the kidneys (**Fig. 7**). Based on the promise displayed, a pilot study of Iopamidol-based quantitative pH-imaging was performed by Muller-Lutz and colleagues in 2013, by measuring in vivo the pH in the bladder of a healthy volunteer with a clinical 3T scanner and showing a good agreement with the urine pH measured by a pH-meter [117]. In addition, the first map of kidney pH was published on a healthy subject at 3 T showing the feasibility of this approach for translational studies [118].

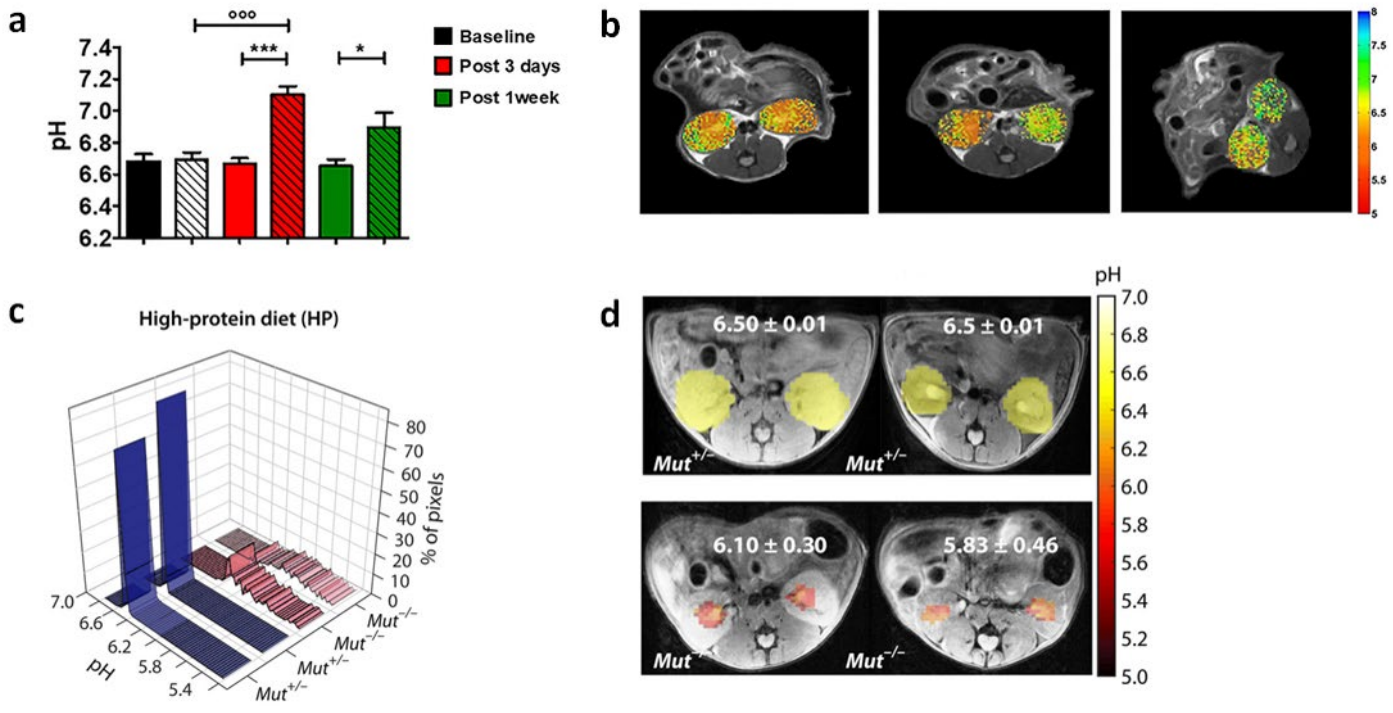

Figure 7. CEST-MRI functional information about renal pH homeostasis. a) Barplots of measured CEST-MRI pH values for the whole kidneys. b) Representative pH maps (for baseline, post-3-day and post-1-week groups, respectively) superimposed onto the T_{2w} images, showing neutral pH values for the clamped kidneys. The arrow shows the clamped kidney. (*$p < 0.05$; ***$p < 0.001$; t test contralateral versus clamped. °°°$p < 0.001$; Bonferroni's test baseline versus clamped). [Reprinted from 32153058] c) pH histograms calculated for two representative HP *Mut*$^{+/-}$ mice and two representative HP *Mut*$^{-/-}$ mice. For HP *Mut*$^{+/-}$ mice, more than 80% of the detected pixels display a mean pH of 6.50, whereas for HP *Mut*$^{-/-}$ mice ($n = 3$), an acidic mean pH of 6.10 to 5.83 was observed. d) Time-averaged pH images of *Mut*$^{+/-}$and *Mut*$^{-/-}$ controls of HP mice. pH was further lowered to 5.83 for the most severely diseased mice. The pH was distributed over a narrow range of 6.50 ± 0.02 for both RD and HP *Mut*$^{+/-}$ mice, while this range significantly increased to ±0.30 and ±0.46 along with a decrease in mean pH for HP *Mut*$^{-/-}$ mice. [Reprinted from [116]].

4.1 Enzyme responsive agents

There are a number of probes which after administration can be altered by key enzymes to highlight pathology, particularly tumor tissue. CEST MRI has been extensively explored for detecting enzymatic activity using CEST agents that are responsive to a particular enzyme. Because very often enzyme catalyzes biochemical reactions that involve the change of chemical groups comprised of exchangeable protons, enzymatic activity (i.e., the conversion from a substrate to a product) will result in CEST signal changes. Compared to other MRI methods, CEST MRI is advantageous because one can use a variety of bioorganic agents, even the natural substrates, as imaging probes. We first demonstrated the use of natural compound cytosine as a CEST agent to probe the enzymatic activity of cytosine deaminase (CDase) [119]. When cytosine is converted to

uracil by CDase, the CEST signal at ~2 ppm (aniline protons) decreases to an extent that is proportional to CDase activity. Following this study, we also successfully developed CEST MRI methods for detecting protein kinase A [120] and deoxycytidine kinase [121]. Using natural compounds to probe enzyme activity provides an efficient way to detect an enzyme without much disturbance to normal cell systems. This strategy was soon implemented by many other research groups for detecting, for example, carboxypeptidase G2 [122] and protease [123]. These studies imply that it is feasible to use the inherently insensitive MRI to detect a low concentration of enzymes in living subjects non-invasively.

Natural compounds typically have small CEST offsets that overlap with endogenous CEST signals (*i.e.,* 1-4 ppm), reducing the detection specificity. To overcome this challenge, much effort has been made to develop synthetic agents with large CEST offsets to improve the specificity of enzyme detection. For instance, Bar-Shir and his colleagues designed and synthesized chemically modified thymidine compounds with a favorable CEST signal at ~5 ppm, attributed to pyrimidine amino protons, at physiological pH. Using the new agents, they successfully used CEST MRI to detect herpes simplex virus type-1 thymidine kinase (HSV1-TK) [124, 125]. Using salicylic acid (SA) (~8-10 ppm) [126] as a building block, Pagel et al. developed a variety of sophisticated enzyme responsive agents, which typically have two or more well-separated CEST signals, for detecting alkaline phosphatase [127], sulfatase and esterase [128], cathepsin B [129], urokinase [130], γ-glutamyl transferase (GGT) [131], and kallikrein 6 (KLK6) [132], which are collectively named catalyCEST MRI.

Beyond the detection of enzymatic activity, such an approach can also be integrated into targeted therapy to obtain enzyme-specific theranostics. We have also conjugated olsalazine (Olsa), an anticancer drug with a CEST signal at 9.8 ppm, to a cell-penetrating peptide (RVRR) to construct a theranostic system (Olsa-RVRR) that is responsive to Furin, an enzyme highly expressed in many aggressive tumors. Olsa-RVRR is reduced by glutathione (GSH) and cleaved by Furin in the cytoplasm of cancer cells resulting in the cleaved Olsa-peptide that spontaneously self-assembles to nanostructures through intermolecular interactions (**Fig. 8**). The self-assembled nanostructures can prevent Olsa from rapid efflux and consequently not only increases the anti-tumor effect significantly but also leads to strong CEST signal at 9.8 ppm.

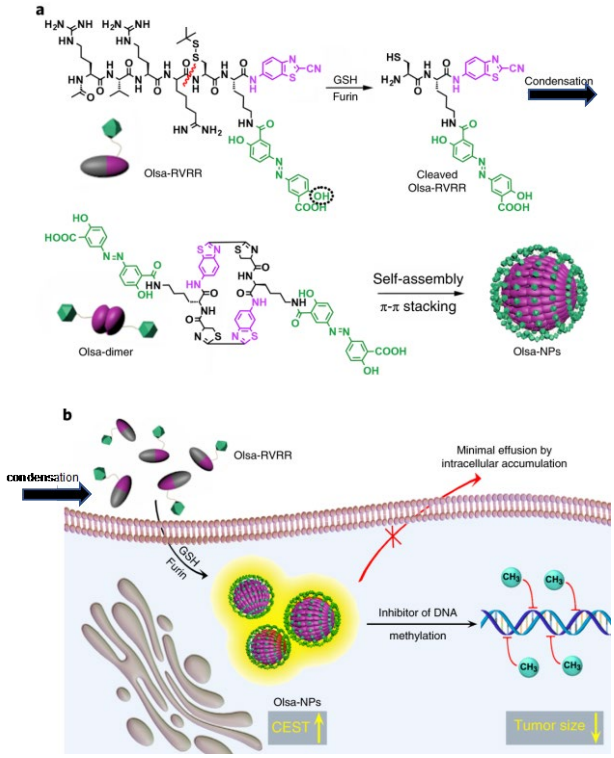

Figure 8. a) Self-assembly of Olsa-RVRR into Olsa-NPs through a series of steps. Red line indicates the site of furin cleavage, and the circled hydroxyl group indicates the exchangeable hydroxyl proton that provides OlsaCEST signal at 9.8 ppm from the water frequency. **b**) After Olsa-RVRR enters the cytoplasm of high furin-expressing cells (HCT116 cells in this study), it undergoes reduction by GSH and cleavage of the peptide by furin near the Golgi complex where cleaved Olsa-RVRR is generated. Amphiphilic oligomers (mostly dimers) are then formed from the click reaction between two cleaved Olsa-RVRR molecules, followed by self-assembly into Olsa-NPs as a result of intermolecular π-π stacking. The intracellular accumulation of Olsa-NPs then serves as a reservoir of Olsa molecule-enhancing CEST contrast and inhibiting DNA methylation for tumor therapy. Reprinted from Ref [133].

5.0 Theranostics

The use of theranostics represents a strategy to integrate imaging into drug treatment[134-136] and has become an emerging approach for carrying out targeted and individualized therapies for various diseases. In the last decade, numerous theranostic systems have been reported for the simultaneous detection and treatment of diseases by specific biomarkers or monitoring the delivery and release of drugs in real-time [137]. In most of these studies, the theranostic systems were constructed in such a way that imaging probes are integrated into drug delivery carriers, either chemically or physically. While this approach has been successfully demonstrated in many preclinical studies, it poses a potential shortcoming: the addition of imaging probes will unavoidably influence the pharmacokinetics of the drug delivery systems, not to mention this may also result in false signal if the imaging probes disassociate from the delivery systems in vivo. Hence, it is highly desirable to construct theranostic systems without imaging labels, so-called label-free theranostics. In this regard, CEST MRI has been exploited to make otherwise MRI invisible drugs imageable. It is because many drugs possess exchangeable protons that are detectable in CEST MRI. By screening a

library of anticancer drugs, our group first showed that many chemotherapeutic agents, including pyrimidine analogs, purine analogs, and antifolates, can generate CEST MRI contrast, permitting detection of these label-free theranostics[138]. In the study, we demonstrated the CEST MRI detection of uptake and distribution of i.v.-injected a liposomal form of gemcitabine (a first-line anticancer drug for pancreatic cancers) in experimental tumors in mice. Gemcitabine has two strong CEST MRI signals at physiological conditions (pH=7.4 and 37°C, PBS), *i.e.,* 2.2 ppm and 1.0 ppm, corresponding to the amino and hydroxyl protons, respectively. The detection sensitivity was estimated to be <1 mM for PBS samples and 1-2 mM for gel samples, suggesting CEST MRI has a moderate sensitivity in detecting these drugs, which however still has potential in the scenarios where drugs are administered at a relatively high dose. While most CEST MRI studies were conducted using high field scanners, a recent study [139] has shown that CEST MRI could detect gemcitabine that was loaded in hydrogel at 3T, confirming the feasibility of using CEST MRI to detect drugs at low magnetic fields.

Non Steroidal Anti-Inflammatory Drugs (NSAIDs) are in widespread use for the reduction of pain and inflammation. We discovered that a number of salicylates and anthranillates can act as both NSAIDs and as high performance CEST agents with the CEST properties tuned through intramolecular hydrogen bonding [140-142]. We have characterized a number of like compounds which possess labile protons with chemical shifts between 5 – 12 ppm from water including the ones shown in **Fig. 9** which allows outstanding detection sensitivity for a variety of magnetic field strengths. Since the labile protons resonate > 4 ppm from water, there is minimal overlap with endogenous CEST agents which should maximize the potential for quantification. Another attractive feature of salicylate and anthranillate agents is the wealth of literature on pharmacokinetics and toxicity. For example, SA is a known NSAID, the active metabolite of aspirin, a key ingredient in many skin-care products, and part of human diets [143]. 4-amino-SA was introduced to clinical use in 1948 as an antibiotic for tuberculosis treatment [144] and is administered (PASER ®) to patients at a dosage of 4 grams 3 times a day. 5-amino-SA is an NSAID administered for treatment of inflammatory bowel disease. 2,4-dihydrobenzoic acid is a metabolite found in blood plasma after drinking cranberry juice [145]. Other salicylates and anthranillates used as drugs include diflunisal, olsalazine, balsalazide, olksalazine, sulfasalazin, pamoic acid, flufenamic acid and meclofenamic acid. Separate from their capabilities for pain and inflammation, a number of studies have found these salicylates inhibit development of cancer[146], and in fact we have recently shown that injectable aspirin can be used to for breast cancer imaging as its metabolite is well detected in these tumors [147]. It is also possible to derivatize the anthranillates and still retain

large chemical shifts on the labile protons, with Hydrazo-CEST probes being one example [148, 149]. The acetanilides are other similar compounds which form intermolecular hydrogen bonds resulting in well tuned proton exchange [150]. Based on their favorable exchange properties, it is expected that several of these agents find use on clinical 3 T scanners.

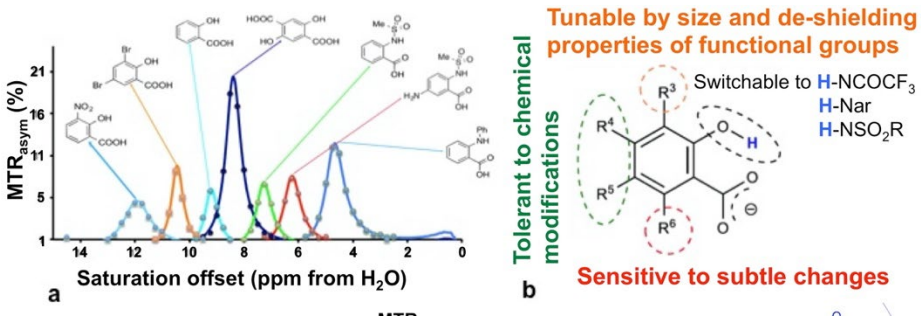

Figure 9. Select salicylate and anthranillate CEST agents. A) 7 of these agents with labile protons resonating between 5 – 12 ppm from water; b) general scaffold for these agents, with MRI properties tolerant to conjugation at R4, R5; Reprinted from Ref [151]

At this point, besides the above mentioned primidne and purine analogs and NSAIDS, label-free CEST-guided drug delivery or CEST theranostics have been demonstrated on a wide spectrum of drugs, e.g., anticancer drugs, including cytarabine [138], decitabine [138], azacitidine [138], fludarabine [138], methotrexate and pemetrexed [51, 138], melphalan [152], olsalazine [133], porphyrins (TPPS4) [33]; NSAIDs including anthranilic acid (Flufenamic acid) [153] and salicylic acid [126], and aspirin [147]; neuroprotective drug citicoline [154], anti-viral drugs, lamivudine (3TC) and emtricitabine (FTC)[155]; cardiovascular drug acebutolol [156]; and even therapeutic bacteria and virus, including clostridium-*NT* [157] and oncolytic herpes simplex virus (HSV)[158]. Collectively, those studies demonstrated the ability of CEST MRI to directly and assess the efficiency of delivery and visualize the biodistribution of drugs and biologics without the need for chemical labeling. It is expected such a label-free theranostic strategy can have an immediate clinical impact.

6.0 Summary

As a very wide range of molecules have labile protons, it is important to understand which have suitable protons with the appropriate chemical exchange rates (k_{ex}) at physiologically relevant pH values and chemical shift differences with water ($\Delta\omega$). The two-pool Bloch-McConnell equations using a long saturation pulse can be numerically solved to characterize how the CEST contrast depends on k_{ex}, $\Delta\omega$, saturation field strength (ω_1) and number of labile protons per molecule as has been mentioned previously [151]. In Fig. 10 and Table 1 we list the k_{ex} and $\Delta\omega$ for a

set of diaCEST agents tested for various medical applications. As can be seen, the chemical shift of the porphyrins including TPPS4 can be highly upfield shifted and thus has a unique feature. As we move downfield from water, there are endogenous metabolites Glucose, Glutamate and creatine which have a chemical shift within 3 ppm, where Glutamate and Creatine have labile amine group protons and Glucose has has labile hydroxyl group protons. Iopamidol has multiple labile protons and lies within 6 ppm from water. I45DC-diGlu also has multiple labile and located further downfield. Salicylic acid and Olsalazine have chemical shifts closer to 10 ppm.

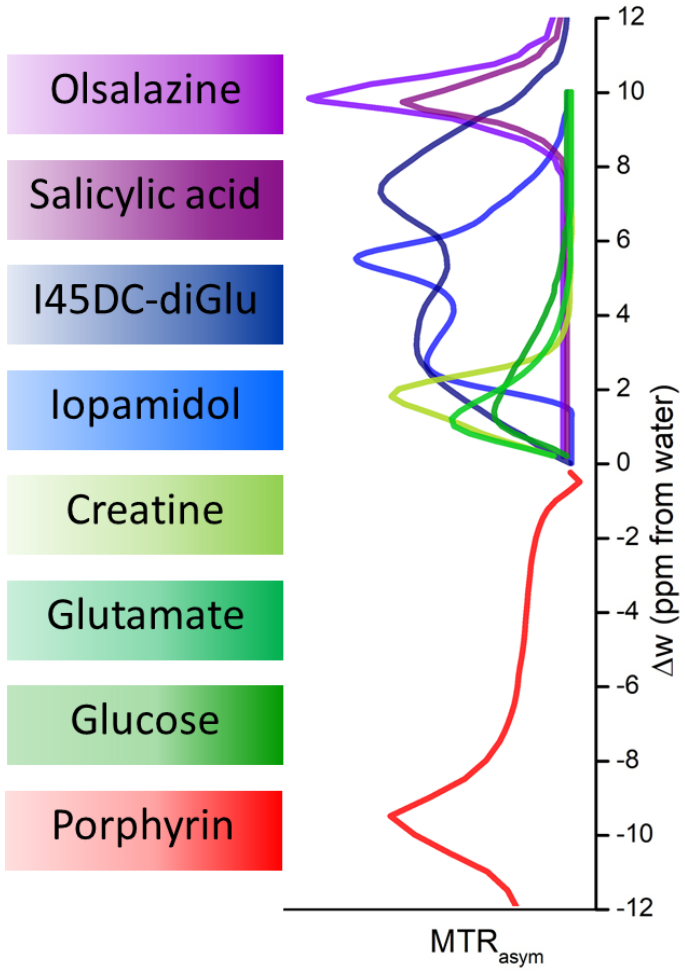

Figure 10: CEST MTR_{asym} spectra for common diaCEST agents described in this review.

In **Figure 11**, select diaCEST agents we describe in this review are inserted into a plot of our Bloch simulations to demonstrate their expected relative sensitivities at two field strengths, 11.7 T and 3 T, using 3 sec saturation pulses at two saturation field strengths: 4 μT and 6 μT. This is an imperfect depiction, as some agents have many more exchangeable protons, for example glucose has six per molecule and olsalazine has two while salicylic acid has only one. Nevertheless, what can be seen is that the detection is expected to improve at the higher filed strength, 11.7 T compared

to the widely clinically used 3 T. For example for salicylic acid, olsalazine and $TPPS_4$ porphyrin, the contrast improves ~2 times from 3 T to 11.7 T for B_1= 4 μT and ~4 times from 3T to 11.7 T for

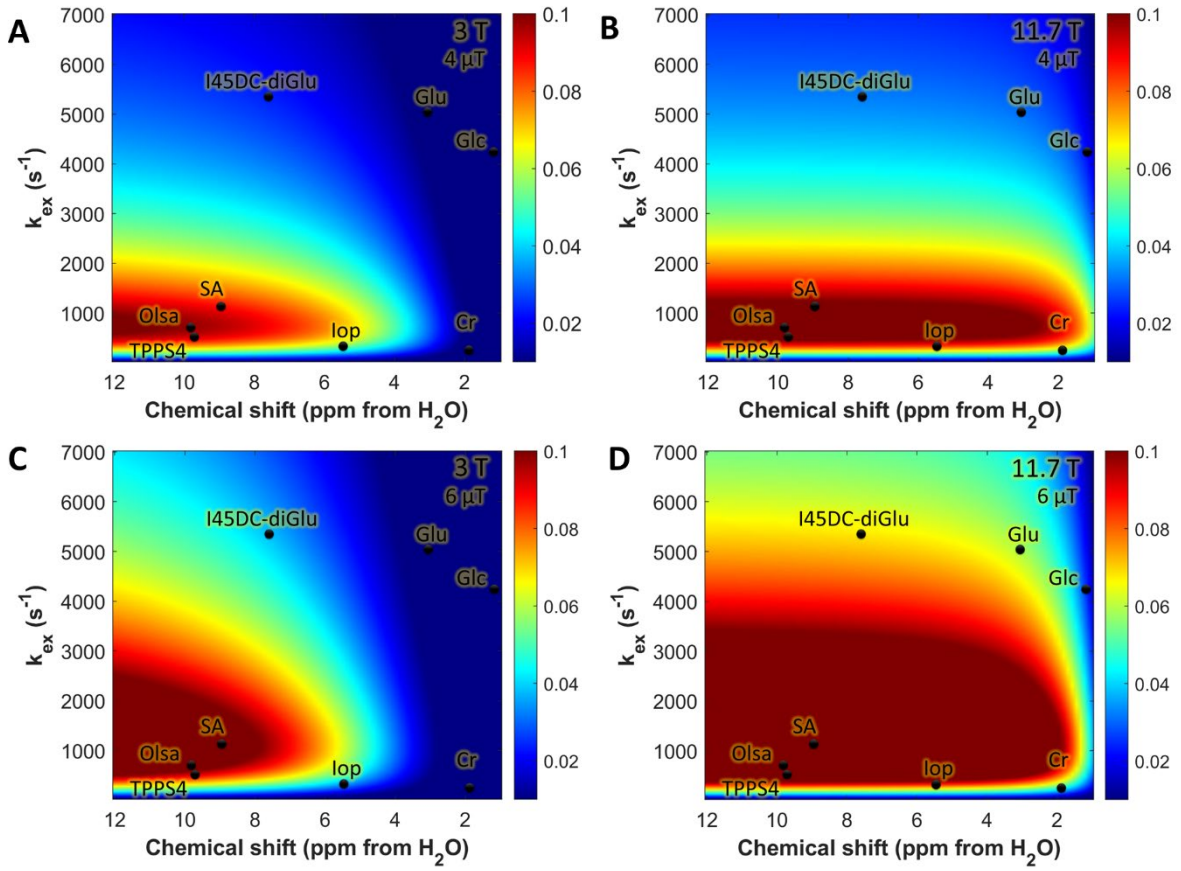

Figure 11: Simulated CEST contrast as function of labile proton chemical shift, Δω and exchange constant, k_{ex} for the following conditions: A) B_0= 3T, ω_1= 4 μT B) B_0= 11.7 T, ω_1= 4 μT C) B_0= 3T, ω_1= 6 μT D) B_0= 11.7 T, ω_1= 6 μT. Simulation parameters: χ_{CA} = 10 mM, T_{1w}=T_{1s} = 4 s, T_{2w} =T_{2s}= 0.1 s TPPS4 = Tetraphenylporphine sulfonate, I45DC-diGlu = 4,5-bis[(Glu)carbonyl]-1H-imidazole

B_1= 6 μT. For Iopamidol, the contrast improves ~11 times from 3T to 11.7 T for 4 μT and ~37 times from 3T to 11.7 T for 6 μT. I45DC-diGlu, the contrast improves ~3 times from 3T to 11.7 T for 4 μT and ~7 times from 3T to 11.7 T for 6 μT. Even for D-Glucose, Creatine and Glutamate, the contrast improved by larger factors with increase in B_0 and B_1. In vivo behavior is not quite so easily predicted of course, and the contrast for these small molecules will depend on the microenvironment for the tissue in which these reside, which will impact exchange and relaxation rates. In fact, this is a positive feature, as changes in environmental pH results in significant differences in contrast for any CEST pH sensor such as iopamidol or I45DC-diGlu enabling the production of pH maps. Other improtant factors include pharmacokinetics of the agent and toxicity of the compounds. Based on all these considerations, different agents may perform better for each application.

Table 1. List of select diaCEST probes along with their exchange properties.

diaCEST contrast agent	*Concentration*	*Bo, B1, t_{sat}*	*Chemical shifts (ppm)*	*pH, T*	*Exchange rate (s^{-1})*	*References*
Porphyrin (TPPS4)	20 mM	9.4 T,3.6 µT, 3s	-9.75	37 ˚C, 6.6	430	Zhang et al, 2019
D-Glucose	20mM	9.4 T, 50 ms	1.2	37 ˚C, 6.8	4280	Jin et al, 2014
Glutamate	20 mM	9.4 T, 3.6 µT, 5 s	3	37 ˚C, 7	5000	Cui J, Zu Z, 2019
Creatine	25 mM	11.7 T, 6 µT, 3s	1.9	37 ˚C, 6.5	~175	Pavuluri et al, 2020
Iopamidol	20 mM	4.7 T, 2.5 µT, 5s	4.3,5.5	37 ˚C, 6.5	265	Sun et al, 2014
I45DC-diGlu	25 mM	11.7 T, 5.9 µT, 3 s	4.5,7.8	37 ˚C, 7.5	5300	Yang et, 2016
Salicylic acid	25 mM	11.7 T,7.2 µT,3 s	9.3	37 ˚C, 7	1200	Yang et al, 2013
Olsalazine	10 mM	11.7 T, 3.6 µT, 3 s	9.8	37 ˚C, 7.4	697	Yuan et al, 2019

Reference:

1. Dagher, A.P., Aletras, A., Choyke, P. & Balaban, R.S. Imaging of urea using chemical exchange-dependent saturation transfer at 1.5T. *J Magn Reson Imaging* **12**, 745-748 (2000).
2. Wolff, S.D. & Balaban, R.S. Nmr Imaging of Labile Proton-Exchange. *J Magn Reson* **86**, 164-169 (1990).
3. Goffeney, N., Bulte, J.W., Duyn, J., Bryant, L.H., Jr. & van Zijl, P.C. Sensitive NMR detection of cationic-polymer-based gene delivery systems using saturation transfer via proton exchange. *J Am Chem Soc* **123**, 8628-8629 (2001).
4. Ward, K.M., Aletras, A.H. & Balaban, R.S. A new class of contrast agents for MRI based on proton chemical exchange dependent saturation transfer (CEST). *Journal of Magnetic Resonance* **143**, 79-87 (2000).
5. Snoussi, K., Bulte, J.W., Gueron, M. & van Zijl, P.C. Sensitive CEST agents based on nucleic acid imino proton exchange: detection of poly(rU) and of a dendrimer-poly(rU) model for nucleic acid delivery and pharmacology. *Magn Reson Med* **49**, 998-1005 (2003).
6. Zhou, J., Lal, B., Wilson, D.A., Laterra, J. & van Zijl, P.C.M. Amide proton transfer (APT) contrast for imaging of brain tumors. *Magnetic Resonance in Medicine* **50**, 1120-1126 (2003).
7. McMahon, M.T., Gilad, A.A., Bulte, J.W.M. & van Zijl, P.C.M. Chemical Exchange Saturation Transfer Imaging: Advances and Applications, Edn. 1st. (Pan Stanford Publishing, Singapore; 2017).
8. Rivlin, M. & Navon, G. Molecular imaging of tumors by chemical exchange saturation transfer MRI of glucose analogs. *Quantitative imaging in medicine and surgery* **9**, 1731-1746 (2019).
9. Walker-Samuel, S. et al. In vivo imaging of glucose uptake and metabolism in tumors. *Nature Medicine* (2013).
10. Chan, K.W. et al. Natural D-glucose as a biodegradable MRI contrast agent for detecting cancer. *Magnetic resonance in medicine : official journal of the Society of Magnetic Resonance in Medicine / Society of Magnetic Resonance in Medicine* **68**, 1764-1773 (2012).
11. Capozza, M. et al. GlucoCEST MRI for the Evaluation Response to Chemotherapeutic and Metabolic Treatments in a Murine Triple-Negative Breast Cancer: A Comparison with[(18)F]F-FDG-PET. *Mol Imaging Biol* (2021).
12. Rivlin, M., Tsarfaty, I. & Navon, G. Functional molecular imaging of tumors by chemical exchange saturation transfer MRI of 3-O-Methyl-D-glucose. *Magn Reson Med* **72**, 1375-1380 (2014).
13. Anemone, A. et al. In vitro and in vivo comparison of MRI chemical exchange saturation transfer (CEST) properties between native glucose and 3-O-Methyl-D-glucose in a murine tumor model. *NMR Biomed* **34**, e4602 (2021).
14. Wang, J., Fukuda, M., Chung, J.J., Wang, P. & Jin, T. Chemical exchange sensitive MRI of glucose uptake using xylose as a contrast agent. *Magn Reson Med* **85**, 1953-1961 (2021).
15. Jin, T., Mehrens, H., Wang, P. & Kim, S.G. Glucose metabolism-weighted imaging with chemical exchange-sensitive MRI of 2-deoxyglucose (2DG) in brain: Sensitivity and biological sources. *NeuroImage* **143**, 82-90 (2016).
16. Bagga, P. et al. Sugar alcohol provides imaging contrast in cancer detection. *Sci Rep* **9**, 11092 (2019).
17. Haris, M., Cai, K., Singh, A., Hariharan, H. & Reddy, R. In vivo mapping of brain myo-inositol. *NeuroImage* **54**, 2079-2085 (2011).
18. Chan, K.W. et al. CEST-MRI detects metabolite levels altered by breast cancer cell aggressiveness and chemotherapy response. *NMR Biomed* **29**, 806-816 (2016).
19. Liu, G. et al. In vivo multicolor molecular MR imaging using diamagnetic chemical exchange saturation transfer liposomes. *Magnetic Resonance in Medicine* **67**, 1106-1113 (2012).
20. Cai, K. et al. Magnetic resonance imaging of glutamate. *Nature Medicine* **18**, 302-306 (2012).
21. Jin, T., Autio, J., Obata, T. & Kim, S.G. Spin-locking versus chemical exchange saturation transfer MRI for investigating chemical exchange process between water and labile metabolite protons. *Magn Reson Med* **65**, 1448-1460 (2011).
22. Bagga, P. et al. Mapping the alterations in glutamate with GluCEST MRI in a mouse model of dopamine deficiency. *Journal of neurochemistry* **139**, 432-439 (2016).
23. Cai, K.J. et al. Mapping glutamate in subcortical brain structures using high-resolution

GluCEST MRI. *NMR Biomed* **26**, 1278-1284 (2013).
24. Hadar, P.N. et al. Volumetric glutamate imaging (GluCEST) using 7T MRI can lateralize nonlesional temporal lobe epilepsy: A preliminary study. *Brain and behavior* **11**, e02134 (2021).
25. Demetriou, E., Tachrount, M., Zaiss, M., Shmueli, K. & Golay, X. PRO-QUEST: a rapid assessment method based on progressive saturation for quantifying exchange rates using saturation times in CEST. *Magn Reson Med* **80**, 1638-1654 (2018).
26. Chan, K.W.Y. et al. MRI-detectable pH nanosensors incorporated into¬†hydrogels for in¬†vivo sensing of transplanted-cell viability. *Nature materials* **12**, 268-275 (2013).
27. Haris, M. et al. Exchange rates of creatine kinase metabolites: feasibility of imaging creatine by chemical exchange saturation transfer MRI. *NMR in biomedicine* **25**, 1305-1309 (2012).
28. Kogan, F. et al. Method for high-resolution imaging of creatine in vivo using chemical exchange saturation transfer. *Magnetic Resonance in Medicine*, n/a-n/a (2013).
29. Chen, L., Barker, P.B., Weiss, R.G., van Zijl, P.C.M. & Xu, J. Creatine and phosphocreatine mapping of mouse skeletal muscle by a polynomial and Lorentzian line-shape fitting CEST method. *Magn Reson Med* **81**, 69-78 (2019).
30. Rerich, E., Zaiss, M., Korzowski, A., Ladd, M.E. & Bachert, P. Relaxation-compensated CEST-MRI at 7 T for mapping of creatine content and pH--preliminary application in human muscle tissue in vivo. *NMR Biomed* **28**, 1402-1412 (2015).
31. Jiang, W., Zhou, I.Y., Wen, L., Zhou, X. & Sun, P.Z. A theoretical analysis of chemical exchange saturation transfer echo planar imaging (CEST-EPI) steady state solution and the CEST sensitivity efficiency-based optimization approach. *Contrast Media Mol Imaging* **11**, 415-423 (2016).
32. Pavuluri, K., Rosenberg, J.T., Helsper, S., Bo, S. & McMahon, M.T. Amplified detection of phosphocreatine and creatine after supplementation using CEST MRI at high and ultrahigh magnetic fields. *J Magn Reson* **313**, 106703 (2020).
33. Zhang, X. et al. Free-base porphyrins as CEST MRI contrast agents with highly upfield shifted labile protons. *Magn Reson Med* **82**, 577-585 (2019).
34. Chakraborty, S., Das, M., Srinivasan, A. & Ghosh, A. Tetrakis-(N-methyl-4-pyridinium)-porphyrin as a diamagnetic chemical exchange saturation transfer (diaCEST) MRI contrast agent. *New Journal of Chemistry* **45**, 1262-1268 (2021).
35. Vahrmeijer, A.L., Hutteman, M., van der Vorst, J.R., van de Velde, C.J. & Frangioni, J.V. Image-guided cancer surgery using near-infrared fluorescence. *Nature reviews. Clinical oncology* **10**, 507-518 (2013).
36. Pushpan, S.K. et al. Porphyrins in photodynamic therapy - a search for ideal photosensitizers. *Current medicinal chemistry. Anti-cancer agents* **2**, 187-207 (2002).
37. Longo, D.L. et al. EXCI-CEST: Exploiting pharmaceutical excipients as MRI-CEST contrast agents for tumor imaging. *International journal of pharmaceutics* **525**, 275-281 (2017).
38. Li, Y. et al. Characterization of tumor vascular permeability using natural dextrans and CEST MRI. *Magn Reson Med* **79**, 1001-1009 (2018).
39. Liu, G. et al. A dextran-based probe for the targeted magnetic resonance imaging of tumours expressing prostate-specific membrane antigen. *Nat Biomed Eng* **1**, 977-982 (2017).
40. van Zijl, P.C., Jones, C.K., Ren, J., Malloy, C.R. & Sherry, A.D. MRI detection of glycogen in vivo by using chemical exchange saturation transfer imaging (glycoCEST). *Proc Natl Acad Sci U S A* **104**, 4359-4364 (2007).
41. Zhou, Y. et al. Magnetic resonance imaging of glycogen using its magnetic coupling with water. *Proc Natl Acad Sci U S A* **117**, 3144-3149 (2020).
42. Consolino, L., Irrera, P., Romdhane, F., Anemone, A. & Longo, D.L. Investigating plasma volume expanders as novel macromolecular MRI-CEST contrast agents for tumor contrast-enhanced imaging. *Magn Reson Med* **86**, 995-1007 (2021).
43. Han, Z. & Liu, G. Sugar-based biopolymers as novel imaging agents for molecular magnetic resonance imaging. *Wiley Interdiscip Rev Nanomed Nanobiotechnol* **11**, e1551 (2019).
44. Chen, H. et al. CEST MRI monitoring of tumor response to vascular disrupting therapy using high molecular weight dextrans. *Magn Reson Med* **82**, 1471-1479 (2019).
45. Han, Z. et al. Extradomain-B Fibronectin-Targeted Dextran-Based Chemical Exchange Saturation Transfer Magnetic Resonance Imaging Probe for Detecting Pancreatic Cancer.

Bioconjug Chem **30**, 1425-1433 (2019).
46. Zhou, Y., van Zijl, P.C.M., Xu, J. & Yadav, N.N. Mechanism and quantitative assessment of saturation transfer for water-based detection of the aliphatic protons in carbohydrate polymers. *Magn Reson Med* **85**, 1643-1654 (2021).
47. Chan, K.W. et al. A diaCEST MRI approach for monitoring liposomal accumulation in tumors. *Journal of controlled release : official journal of the Controlled Release Society* **180**, 51-59 (2014).
48. Yu, T. et al. Liposome-based mucus-penetrating particles (MPP) for mucosal theranostics: demonstration of diamagnetic chemical exchange saturation transfer (diaCEST) magnetic resonance imaging (MRI). *Nanomedicine* **11**, 401-405 (2015).
49. Han, X. et al. CEST MRI detectable liposomal hydrogels for multiparametric monitoring in the brain at 3T. *Theranostics* **10**, 2215-2228 (2020).
50. Demetriou, E. et al. Effect of Liposomal Encapsulation on the Chemical Exchange Properties of Diamagnetic CEST Agents. *The journal of physical chemistry. B* **123**, 7545-7557 (2019).
51. Lock, L.L. et al. One-Component Supramolecular Filament Hydrogels as Theranostic Label-Free Magnetic Resonance Imaging Agents. *ACS Nano* **11**, 797-805 (2017).
52. Chan, K.W. et al. MRI-detectable pH nanosensors incorporated into hydrogels for in vivo sensing of transplanted-cell viability. *Nat Mater* **12**, 268-275 (2013).
53. Jin, T. et al. Diamagnetic chemical exchange saturation transfer (diaCEST) affords magnetic resonance imaging of extracellular matrix hydrogel implantation in a rat model of stroke. *Biomaterials* **113**, 176-190 (2017).
54. Lesniak, W.G. et al. Salicylic Acid Conjugated Dendrimers Are a Tunable, High Performance CEST MRI NanoPlatform. *Nano Lett* **16**, 2248-2253 (2016).
55. Gilad, A.A. et al. Artificial reporter gene providing MRI contrast based on proton exchange. *Nat Biotechnol* **25**, 217-219 (2007).
56. McMahon, M.T. et al. New "multicolor" polypeptide diamagnetic chemical exchange saturation transfer (DIACEST) contrast agents for MRI. *Magnetic resonance in medicine : official journal of the Society of Magnetic Resonance in Medicine / Society of Magnetic Resonance in Medicine* **60**, 803-812 (2008).
57. Gatenby, R.A. & Gillies, R.J. Why do cancers have high aerobic glycolysis? *Nat Rev Cancer* **4**, 891-899 (2004).
58. Aime, S., Delli Castelli, D., Fedeli, F. & Terreno, E. A paramagnetic MRI-CEST agent responsive to lactate concentration. *J. Am. Chem. Soc.* **124**, 9364-9365 (2002).
59. Aime, S. et al. Paramagnetic lanthanide(III) complexes as pH-sensitive chemical exchange saturation transfer (CEST) contrast agents for MRI applications. *Magn. Reson. Med.* **47**, 639-648 (2002).
60. Wu, Y.K., Soesbe, T.C., Kiefer, G.E., Zhao, P.Y. & Sherry, A.D. A Responsive Europium(III) Chelate That Provides a Direct Readout of pH by MRI. *J. Am. Chem. Soc.* **132**, 14002-14003 (2010).
61. Delli Castelli, D., Terreno, E. & Aime, S. Yb-III-HPDO3A: A Dual pH- and Temperature-Responsive CEST Agent. *Angew. Chem.-Int. Edit.* **50**, 1798-1800 (2011).
62. Sheth, V.R. et al. Measuring in vivo tumor pHe with CEST-FISP MRI. *Magn. Reson. Med.* **67**, 760-768 (2012).
63. McVicar, N. et al. Simultaneous In Vivo pH and Temperature Mapping Using a PARACEST-MRI Contrast Agent. *Magn. Reson. Med.* **70**, 1016-1025 (2013).
64. Castelli, D.D., Ferrauto, G., Cutrin, J.C., Terreno, E. & Aime, S. In Vivo Maps of Extracellular pH in Murine Melanoma by CEST-MRI. *Magn. Reson. Med.* **71**, 326-332 (2014).
65. Ward, K.M. & Balaban, R.S. Determination of pH using water protons and chemical exchange dependent saturation transfer (CEST). *Magn. Reson. Med.* **44**, 799-802 (2000).
66. Zhou, J., Payen, J.F., Wilson, D.A., Traystman, R.J. & van Zijl, P.C.M. Using the amide proton signals of intracellular proteins and peptides to detect pH effects in MRI. *Nature Medicine* **9**, 1085-1090 (2003).
67. Aime, S. et al. Iopamidol: Exploring the potential use of a well-established X-ray contrast agent for MRI. *Magn. Reson. Med.* **53**, 830-834 (2005).
68. McMahon, M.T. et al. Quantifying exchange rates in chemical exchange saturation transfer agents using the saturation time and saturation power dependencies of the magnetization

transfer effect on the magnetic resonance imaging signal (QUEST and QUESP): Ph calibration for poly-L-lysine and a starburst dendrimer. *Magn Reson Med* **55**, 836-847 (2006).
69. Chan, K.W.Y. et al. MRI-detectable pH nanosensors incorporated into¬†hydrogels for in¬†vivo sensing of transplanted-cell viability. *Nat Mater* **12**, 268-275 (2013).
70. Sun, P.Z., Benner, T., Kumar, A. & Sorensen, A.G. Investigation of optimizing and translating pH-sensitive pulsed-chemical exchange saturation transfer (CEST) imaging to a 3T clinical scanner. *Magn. Reson. Med.* **60**, 834-841 (2008).
71. Wang, H. et al. (1)H NMR-based metabolic profiling of human rectal cancer tissue. *Mol Cancer* **12**, 121 (2013).
72. Chen, L.Q. et al. Evaluations of extracellular pH within in vivo tumors using acidoCEST MRI. *Magn. Reson. Med.*, n/a-n/a (2013).
73. McDonald, R.J. et al. Intravenous contrast material-induced nephropathy: causal or coincident phenomenon? *Radiology* **267**, 106-118 (2013).
74. Orbeck, H. [Bilateral renal cortical necrosis and general Schwartzman reaction. Literature review and case presentation]. *Tidsskrift for den Norske laegeforening : tidsskrift for praktisk medicin, ny raekke* **91**, 1222-1225 (1971).
75. Gillies, R.J., Raghunand, N., Garcia-Martin, M.L. & Gatenby, R.A. pH imaging. *IEEE Engineering in medicine and biology magazine* **23**, 57-64 (2004).
76. Gillies, R.J., Raghunand, N., Karczmar, G.S. & Bhujwalla, Z.M. MRI of the tumor microenvironment. *J Magn Reson Imaging* **16**, 430-450 (2002).
77. Pavuluri, K. & McMahon, M.T. pH imaging using chemical exchange saturation transfer (CEST) MRI. *Israel Journal of Chemistry* **57**, 862-879 (2017).
78. Aime, S., Nano, R. & Grandi, M. A new class of contrast agents for magnetic resonance imaging based on selective reduction of water-T2 by chemical exchange. *Investigative radiology* **23 Suppl 1**, S267-270 (1988).
79. Aime, S. et al. Iopamidol: Exploring the potential use of a well-established x-ray contrast agent for MRI. *Magn Reson Med* **53**, 830-834 (2005).
80. Longo, D.L. et al. Iopamidol as a responsive MRI-chemical exchange saturation transfer contrast agent for pH mapping of kidneys: In vivo studies in mice at 7 T. *Magn Reson Med* **65**, 202-211 (2011).
81. Sun, P.Z., Longo, D.L., Hu, W., Xiao, G. & Wu, R. Quantification of iopamidol multi-site chemical exchange properties for ratiometric chemical exchange saturation transfer (CEST) imaging of pH. *Physics in medicine and biology* **59**, 4493-4504 (2014).
82. Longo, D.L. et al. A general MRI-CEST ratiometric approach for pH imaging: demonstration of in vivo pH mapping with iobitridol. *J Am Chem Soc* **136**, 14333-14336 (2014).
83. Chen, L.Q. et al. Evaluations of extracellular pH within in vivo tumors using acidoCEST MRI. *Magn Reson Med* **72**, 1408-1417 (2014).
84. Moon, B.F. et al. A comparison of iopromide and iopamidol, two acidoCEST MRI contrast media that measure tumor extracellular pH. *Contrast Media Mol Imaging* **10**, 446-455 (2015).
85. Arena, F. et al. Flip-angle based ratiometric approach for pulsed CEST-MRI pH imaging. *J Magn Reson* **287**, 1-9 (2018).
86. Cobb, J.G., Xie, J., Li, K., Gochberg, D.F. & Gore, J.C. Exchange-mediated contrast agents for spin-lock imaging. *Magn Reson Med* **67**, 1427-1433 (2012).
87. Longo, D.L. et al. In Vitro and In Vivo Assessment of Nonionic Iodinated Radiographic Molecules as Chemical Exchange Saturation Transfer Magnetic Resonance Imaging Tumor Perfusion Agents. *Investigative radiology* **51**, 155-162 (2016).
88. Aime, S. & Caravan, P. Biodistribution of Gadolinium-Based Contrast Agents, Including Gadolinium Deposition. *Journal of Magnetic Resonance Imaging* **30**, 1259-1267 (2009).
89. Bennett, C.L. et al. Gadolinium-induced nephrogenic systemic fibrosis: the rise and fall of an iatrogenic disease. *Clinical kidney journal* **5**, 82-88 (2012).
90. Stanescu, A.L. et al. Brain tissue gadolinium retention in pediatric patients after contrast-enhanced magnetic resonance exams: pathological confirmation. *Pediatric Radiology* **50**, 388-396 (2020).
91. Murata, N. et al. Macrocyclic and Other Non–Group 1 Gadolinium Contrast Agents Deposit Low Levels of Gadolinium in Brain and Bone Tissue: Preliminary Results From 9 Patients With Normal Renal Function. *Investigative Radiology* **51**, 447-453 (2016).

92. Bussi, S. et al. Macrocyclic MR contrast agents: evaluation of multiple-organ gadolinium retention in healthy rats. *Insights Imaging* **11**, 11-11 (2020).
93. Quattrocchi, C.C. et al. Gadodiamide and Dentate Nucleus T1 Hyperintensity in Patients With Meningioma Evaluated by Multiple Follow-Up Contrast-Enhanced Magnetic Resonance Examinations With No Systemic Interval Therapy. *Investigative radiology* **50**, 470-472 (2015).
94. Anemone, A., Consolino, L. & Longo, D.L. MRI-CEST assessment of tumour perfusion using X-ray iodinated agents: comparison with a conventional Gd-based agent. *European radiology* **27**, 2170-2179 (2017).
95. Garcia-Martin, M.L. et al. Mapping extracellular pH in rat brain gliomas in vivo by H-1 magnetic resonance spectroscopic imaging: Comparison with maps of metabolites. *Cancer Res.* **61**, 6524-6531 (2001).
96. Provent, P. et al. Serial in vivo spectroscopic nuclear magnetic resonance Imaging of lactate and extracellular pH in rat gliomas shows redistribution of protons away from sites of glycolysis. *Cancer Res.* **67**, 7638-7645 (2007).
97. Yang, X. et al. Developing imidazoles as CEST MRI pH sensors. *Contrast media & molecular imaging* **11**, 304-312 (2016).
98. Lauzon, C.B., van Zijl, P. & Stivers, J.T. Using the water signal to detect invisible exchanging protons in the catalytic triad of a serine protease. *J. Biomol. NMR* **50**, 299-314 (2011).
99. Bachovchin, W.W. Contributions of NMR spectroscopy to the study of hydrogen bonds in serine protease active sites. *Magn. Reson. Chem.* **39**, S199-S213 (2001).
100. Rush, J.R. et al. Intramolecular hydrogen bond strength and pK(a) determination of N,N '-disubstituted imidazole-4,5-dicarboxamides. *Org. Lett.* **7**, 135-138 (2005).
101. Baures, P.W. et al. Intramolecular hydrogen bonding and intermolecular dimerization in the crystal structures of imidazole-4,5-dicarboxylic acid derivatives. *Cryst. Growth Des.* **2**, 653-664 (2002).
102. L.T., K. Pharmacological activity and toxicity of neurotropic agents in experimental hypodynamia. *Farmakol Toksikol* **42**, 221-225 (1979).
103. Kniga, M. *Farmakol Toksikol* **22**, 11 (1959).
104. Ibrahim-Hashim, A. & Estrella, V. Acidosis and cancer: from mechanism to neutralization. *Cancer metastasis reviews* **38**, 149-155 (2019).
105. Vaupel, P., Schmidberger, H. & Mayer, A. The Warburg effect: essential part of metabolic reprogramming and central contributor to cancer progression. *International journal of radiation biology* **95**, 912-919 (2019).
106. Longo, D.L. et al. In Vivo Imaging of Tumor Metabolism and Acidosis by Combining PET and MRI-CEST pH Imaging. *Cancer Res* **76**, 6463-6470 (2016).
107. Pillai, S.R. et al. Causes, consequences, and therapy of tumors acidosis. *Cancer metastasis reviews* **38**, 205-222 (2019).
108. Anemone, A. et al. In vivo evaluation of tumour acidosis for assessing the early metabolic response and onset of resistance to dichloroacetate by using magnetic resonance pH imaging. *International journal of oncology* **51**, 498-506 (2017).
109. Goldenberg, J.M., Cárdenas-Rodríguez, J. & Pagel, M.D. Preliminary Results that Assess Metformin Treatment in a Preclinical Model of Pancreatic Cancer Using Simultaneous [(18)F]FDG PET and acidoCEST MRI. *Mol Imaging Biol* **20**, 575-583 (2018).
110. Anemone, A. et al. Tumour acidosis evaluated in vivo by MRI-CEST pH imaging reveals breast cancer metastatic potential. *British journal of cancer* **124**, 207-216 (2021).
111. Wu, H. et al. T-cells produce acidic niches in lymph nodes to suppress their own effector functions. *Nature communications* **11**, 4113 (2020).
112. Jones, K.M. et al. Clinical Translation of Tumor Acidosis Measurements with AcidoCEST MRI. *Mol Imaging Biol* **19**, 617-625 (2017).
113. Longo, D.L., Busato, A., Lanzardo, S., Antico, F. & Aime, S. Imaging the pH evolution of an acute kidney injury model by means of iopamidol, a MRI-CEST pH-responsive contrast agent. *Magn Reson Med* **70**, 859-864 (2013).
114. Longo, D.L., Cutrin, J.C., Michelotti, F., Irrera, P. & Aime, S. Noninvasive evaluation of renal pH homeostasis after ischemia reperfusion injury by CEST-MRI. *NMR Biomed* **30** (2017).
115. Irrera, P., Consolino, L., Cutrin, J.C., Zöllner, F.G. & Longo, D.L. Dual assessment of kidney perfusion and pH by exploiting a dynamic CEST-MRI approach in an acute kidney ischemia-

reperfusion injury murine model. *NMR Biomed* **33**, e4287 (2020).
116. Pavuluri, K. et al. Noninvasive monitoring of chronic kidney disease using pH and perfusion imaging. *Science advances* **5**, eaaw8357 (2019).
117. Müller-Lutz, A. et al. Pilot study of Iopamidol-based quantitative pH imaging on a clinical 3T MR scanner. *Magma (New York, N.Y.)* **27**, 477-485 (2014).
118. Bo, S. et al. Dynamic Contrast Enhanced-MR CEST Urography: An Emerging Tool in the Diagnosis and Management of Upper Urinary Tract Obstruction. *Tomography (Ann Arbor, Mich.)* **7**, 80-94 (2021).
119. Liu, G. et al. Monitoring enzyme activity using a diamagnetic chemical exchange saturation transfer magnetic resonance imaging contrast agent. *J Am Chem Soc* **133**, 16326-16329 (2011).
120. Airan, R.D. et al. MRI biosensor for protein kinase A encoded by a single synthetic gene. *Magn Reson Med* **68**, 1919-1923 (2012).
121. Han, Z. et al. Molecular Imaging of Deoxycytidine Kinase Activity Using Deoxycytidine-Enhanced CEST MRI. *Cancer Res* **79**, 2775-2783 (2019).
122. Jamin, Y., Eykyn, T.R., Poon, E., Springer, C.J. & Robinson, S.P. Detection of the prodrug-activating enzyme carboxypeptidase G2 activity with chemical exchange saturation transfer magnetic resonance. *Mol Imaging Biol* **16**, 152-157 (2014).
123. Haris, M. et al. In vivo magnetic resonance imaging of tumor protease activity. *Sci Rep* **4**, 6081 (2014).
124. Bar-Shir, A. et al. Transforming thymidine into a magnetic resonance imaging probe for monitoring gene expression. *J Am Chem Soc* **135**, 1617-1624 (2013).
125. Bar-Shir, A., Liu, G., Greenberg, M.M., Bulte, J.W. & Gilad, A.A. Synthesis of a probe for monitoring HSV1-tk reporter gene expression using chemical exchange saturation transfer MRI. *Nat Protoc* **8**, 2380-2391 (2013).
126. Yang, X. et al. Salicylic acid and analogues as diaCEST MRI contrast agents with highly shifted exchangeable proton frequencies. *Angewandte Chemie* **52**, 8116-8119 (2013).
127. Daryaei, I., Ghaffari, M.M., Jones, K.M. & Pagel, M.D. Detection of Alkaline Phosphatase Enzyme Activity with a CatalyCEST MRI Biosensor. *ACS Sens* **1**, 857-861 (2016).
128. Fernandez-Cuervo, G., Sinharay, S. & Pagel, M.D. A CatalyCEST MRI Contrast Agent that Can Simultaneously Detect Two Enzyme Activities. *Chembiochem* **17**, 383-387 (2016).
129. Hingorani, D.V. et al. A single diamagnetic catalyCEST MRI contrast agent that detects cathepsin B enzyme activity by using a ratio of two CEST signals. *Contrast Media Mol Imaging* **11**, 130-138 (2016).
130. Sinharay, S., Howison, C.M., Baker, A.F. & Pagel, M.D. Detecting in vivo urokinase plasminogen activator activity with a catalyCEST MRI contrast agent. *NMR Biomed* **30** (2017).
131. Sinharay, S. et al. Noninvasive detection of enzyme activity in tumor models of human ovarian cancer using catalyCEST MRI. *Magn Reson Med* **77**, 2005-2014 (2017).
132. Sinharay, S., Randtke, E.A., Howison, C.M., Ignatenko, N.A. & Pagel, M.D. Detection of Enzyme Activity and Inhibition during Studies in Solution, In Vitro and In Vivo with CatalyCEST MRI. *Mol Imaging Biol* **20**, 240-248 (2018).
133. Yuan, Y. et al. Furin-mediated intracellular self-assembly of olsalazine nanoparticles for enhanced magnetic resonance imaging and tumour therapy. *Nat Mater* **18**, 1376-1383 (2019).
134. Chen, X.S. Introducing Theranostics Journal - From the Editor-in-Chief. *Theranostics* **1**, 1-2 (2011).
135. Choi, K.Y., Liu, G., Lee, S. & Chen, X. Theranostic nanoplatforms for simultaneous cancer imaging and therapy: current approaches and future perspectives. *Nanoscale* **4**, 330-342 (2012).
136. Shi, J., Kantoff, P.W., Wooster, R. & Farokhzad, O.C. Cancer nanomedicine: progress, challenges and opportunities. *Nat Rev Cancer* **17**, 20-37 (2017).
137. Blau, R., Krivitsky, A., Epshtein, Y. & Satchi-Fainaro, R. Are nanotheranostics and nanodiagnostics-guided drug delivery stepping stones towards precision medicine? *Drug Resist Updat* **27**, 39-58 (2016).
138. Li, Y. et al. CEST theranostics: label-free MR imaging of anticancer drugs. *Oncotarget* **7**, 6369-6378 (2016).
139. Han, X. et al. Imaging Self-Healing Hydrogels and Chemotherapeutics Using CEST MRI at

3 T. *ACS Applied Bio Materials* **4**, 5605-5616 (2021).
140. Yang, X. et al. Salicylic Acid and Analogs: Diamagnetic Chemical Exchange Satuation Transfer (diaCEST) Magnetic Resonance Imaging (MRI) Contrast Agents with Highly Shifted Exchangeable Protons. *Angew. Chemie. Int. Ed.* (2013).
141. Song, X., Yang, X., Ray Banerjee, S., Pomper, M.G. & McMahon, M.T. Anthranilic acid analogues as diamagnetic CEST (diaCEST) MRI contrast agents that feature an IntraMolecular-bond Shifted HYdrogen (IM-SHY) *Con Med & Mol Imag* (2014 doi: 10.1002/cmmi.1597).
142. Li, J. et al. Chemical Exchange Saturation Transfer (CEST) Agents: Quantum Chemistry and MRI. *Chemistry (Weinheim an der Bergstrasse, Germany)* **22**, 264-271 (2016).
143. Paterson, J.R. et al. Salicylic Acid sans Aspirin in Animals and Man: Persistence in Fasting and Biosynthesis from Benzoic Acid. *Journal of Agricultural and Food Chemistry* **56**, 11648-11652 (2008).
144. Lehmann, J. PARA-AMINOSALICYLIC ACID IN THE TREATMENT OF TUBERCULOSIS. *Lancet* **250**, 15-16 (1946).
145. Zhang, K. & Zuo, Y. GC-MS Determination of Flavonoids and Phenolic and Benzoic Acids in Human Plasma after Consumption of Cranberry Juice. *Journal of Agricultural and Food Chemistry* **52**, 222-227 (2004).
146. Rainsford, K. et al. (eds.) Aspirin and Related Drugs. (CRC Press, Boca Raton; 2004).
147. Pavuluri, K. et al. Unlabeled Aspirin as an Activatable Theranostic MRI Agent for Breast Cancer *Theranostics*.
148. Dang, T. et al. Hydrazo-CEST: Hydrazone-Dependent Chemical Exchange Saturation Transfer Magnetic Resonance Imaging Contrast Agents. *Chemistry (Weinheim an der Bergstrasse, Germany)* **24**, 9148-9156 (2018).
149. Brun, E.M.S.P.-T. et al. Mapping vitamin B 6 metabolism by hydrazoCEST magnetic resonance imaging. *Chemical Communications* **57**, 10867-10870 (2021).
150. Chakraborty, S., Peruncheralathan, S. & Ghosh, A. Paracetamol and other acetanilide analogs as inter-molecular hydrogen bonding assisted diamagnetic CEST MRI contrast agents. *RSC Advances* **11**, 6526-6534 (2021).
151. Yang, X. et al. Tuning Phenols with Intra-Molecular Bond Shifted HYdrogens (IM-SHY) as diaCEST MRI Contrast Agents. *Chemistry-a European Journal* **20**, 15824-15832 (2014).
152. Ngen, E.J. et al. Imaging the DNA Alkylator Melphalan by CEST MRI: An Advanced Approach to Theranostics. *Mol Pharm* **13**, 3043-3053 (2016).
153. Song, X., Yang, X., Ray Banerjee, S., Pomper, M.G. & McMahon, M.T. Anthranilic acid analogs as diamagnetic CEST MRI contrast agents that feature an intramolecular-bond shifted hydrogen. *Contrast Media Mol Imaging* **10**, 74-80 (2015).
154. Grieb, P. Neuroprotective properties of citicoline: facts, doubts and unresolved issues. *CNS Drugs* **28**, 185-193 (2014).
155. Bade, A.N., Gendelman, H.E., McMillan, J. & Liu, Y. Chemical exchange saturation transfer for detection of antiretroviral drugs in brain tissue. *AIDS* **35**, 1733-1741 (2021).
156. Fenniche, S. et al. Acebutolol-induced subacute cutaneous lupus erythematosus. *Skin Pharmacol Physiol* **18**, 230-233 (2005).
157. Liu, G. et al. Noninvasive imaging of infection after treatment with tumor-homing bacteria using Chemical Exchange Saturation Transfer (CEST) MRI. *Magn Reson Med* **70**, 1690-1698 (2013).
158. Farrar, C.T. et al. Establishing the Lysine-rich Protein CEST Reporter Gene as a CEST MR Imaging Detector for Oncolytic Virotherapy. *Radiology* **275**, 746-754 (2015).